Earth Planet. Sci. Lett. 690 (2026) 120113

Contents lists available at ScienceDirect

Earth and Planetary Science Letters

journal homepage: www.elsevier.com/locate/epsl

Swarm cessation and aftershock drivers following the pressure release of a four-year-long seismic sequence at the Noto Peninsula

Saeed Mohanna [a], Lingsen Meng [a,*], Alessandro Vuan [b,c], Hongyu Yu [d]

[a] Department of Earth, Planetary and Space Sciences, University of California, Los Angeles, Los Angeles, CA, USA
[b] National Institute of Oceanography and Applied Geophysics—OGS (Italy), Trieste, Italy
[c] Istituto Nazionale di Geofisica e Vulcanologia (Italy), Rome, Italy
[d] School of Earth Sciences, Zhejiang University, Hangzhou 310058, China

ARTICLE INFO

Edited By: Dr H Thybo

Keywords:
Swarms
Coulomb
Background seismicity
Template-matching
Pore fluid pressure

ABSTRACT

We investigated the interplay of seismic and aseismic processes during the 2024 M_w 7.5 Noto Peninsula earthquake sequence. Comparing pore fluid pressure evolution from prior swarm activity with Coulomb stress perturbations from the 2023 M_w 6.3 sequence, we find that high pore pressure likely played a more significant role in triggering the 2024 mainshock than elastic triggering. Using our template matching catalog for the 2024 sequence and existing slip models, we show that physical drivers vary spatially. To validate our interpretations, we modeled the temporal evolution of background seismicity rates in the 2020–2025 Japan Meteorological Agency catalog. Static stress changes from the mainshock contributed to early seismicity, with strong effects in the southwest. The southwest and central zones exhibit signs of migrating afterslip, while the northeastern seismicity is primarily driven by more localized afterslip. Using evidence of swarm cessation in the central zone, we found that the Noto Peninsula experienced poroelastic rebound effects after pressure release, consistent with a cyclical fault-valving mechanism.

1. Introduction

Earthquake sequences typically follow a mainshock–aftershock pattern, in which numerous smaller aftershocks follow a large-magnitude earthquake (the mainshock). The frequency-magnitude distribution of an earthquake sequence typically follows the Gutenberg-Richter law (Gutenberg and Richter, 1944) while the temporal decay of aftershocks is well-described by the Omori–Utsu law (Omori, 1894; Utsu, 1961). In some sequences, however, there is no clear mainshock, but many earthquakes of similar size that occur over time. These are referred to as seismic swarms. While the distinction between swarm-like and mainshock–aftershock sequences is not always clear-cut, seismic catalogs can be analyzed to assess the dominant pattern. Understanding these patterns provides insight into the physical mechanisms that drive seismicity – swarms are typically associated with crustal fluid migration, while mainshock-aftershock sequences result from tectonic loading and subsequent elastic stress triggering.

One of these swarm-like sequences is the 2020–2024 Noto Peninsula sequence in central Japan, near the boundary between the Amur and Okhotsk tectonic plates (Fig. 1). This sequence initially exhibited swarm behavior that began in late 2020, with increasing seismicity in 2021 and 2022. The swarm included episodes of upward earthquake migration from ~15 km depth to shallower levels, largely attributed to fluid migration (Amezawa et al., 2023; Nishimura et al., 2023; Yoshida et al., 2023a, 2023b), related to fault-valve behavior (Kato, 2024). In mid-2023, the sequence began to show mainshock-aftershock characteristics, marked by a M_w 6.3 earthquake followed by hundreds of smaller events.

On January 1, 2024, at 16:10:22 local time, a M_w 7.5 earthquake struck, with the Japan Meteorological Agency (JMA) locating the hypocenter at 37.496°N, 137.270°E, 15.9 km depth. This event triggered a tsunami with an estimated maximum inundation of ~5.5 m (Yuhi et al., 2024), causing 299 fatalities and 1208 injuries (Ishikawa Prefectural Government, 2024). The aftershocks of the M_w 7.5 event extended southwest and offshore to the northeast, contrasting with the preceding years' seismicity, which had been largely confined on land to the northeastern portion of the peninsula.

This sequence provides a unique opportunity to examine the role of different physical mechanisms in earthquake sequences over time. Seismic catalogs are typically analyzed in space and time to track

* Corresponding author.
E-mail address: lsmeng@g.ucla.edu (L. Meng).

https://doi.org/10.1016/j.epsl.2026.120113
Received 8 July 2025; Received in revised form 9 May 2026; Accepted 13 May 2026
Available online 26 May 2026

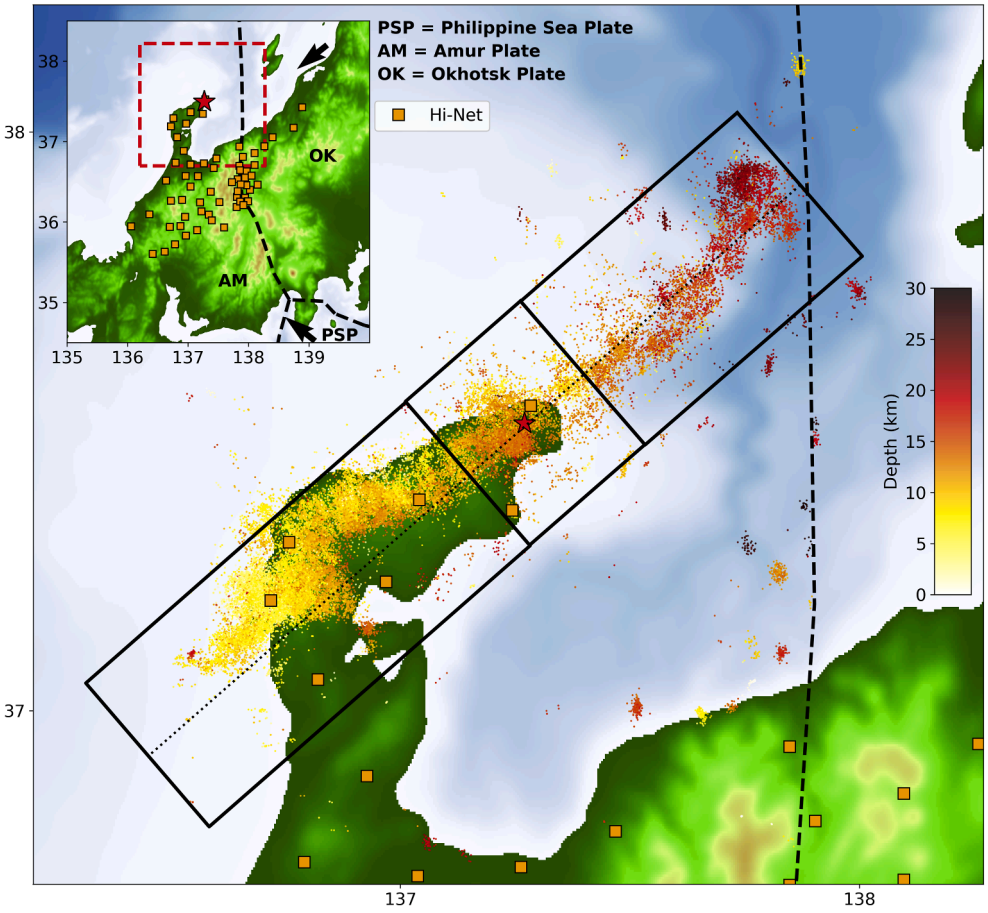

Fig. 1. Map showing all events in our obtained seismicity catalog from 2023/12/01 to 2024/02/02 on the Noto Peninsula, colored by depth. Orange squares show the location of Hi-Net seismometers used to detect earthquake signals. The top left inset shows Japan's regional tectonics with general plate motion directions from the USGS (U.S. Geological Survey, n.d.). The black rectangles show the different zones we examine in Fig. 3.

earthquake migration patterns. To improve precision, resolution is enhanced by detecting more lower magnitude earthquakes. This can be achieved using an advanced detection technique known as template matching (e.g., Gibbons and Ringdal, 2006; Shelly et al., 2007; Vuan et al., 2018).

Peng et al. (2025)'s analysis of the spatiotemporal evolution of the relocated JMA catalog suggests that seismicity along dip followed a diffusive expansion that began in late 2020 with a possible reinjection or change in diffusivity in early 2021. However, the seismicity later that year cannot be fully explained by this diffusive front, suggesting that other processes, such as aseismic slip or stress changes, drove the seismicity thereafter. Kato (2024) identified fluid upwelling as a possible cause of the rapid migration of early aftershocks following the 2023 M_w 6.3 Noto earthquake. Ishikawa and Bai (2024) argue that the faulting orientation in the Noto peninsula prevented fluids from spreading over a wide area in the horizontal plane, leading to a build-up of fluid pressure and thus, decrease in fault strength that triggered the 2024 M_w 7.5 Noto earthquake. Yang et al. (2024) found evidence of afterslip in the first 19 days following the 2024 mainshock that matched with aftershock locations and argued that afterslip may play an important role in driving those events.

Our goal was to assess in more quantitative detail the spatiotemporal contribution of fluid migration, aseismic slip, and elastic stress triggering to this sequence. To ensure robustness in our analysis, we integrate multiple independent approaches. First, we calculate changes in fault strength due to pore pressure perturbations and Coulomb stress changes in the months preceding the 2024 mainshock. Then, we refine the JMA earthquake catalog using a template-matching technique over a two-month period, spanning one month before and one month after the 2024 mainshock. Using this enhanced catalog and postseismic deformation models, we obtain the spatial distribution of the seismic-to-geodetic ratio, which can be used to map in finer detail the spatial distribution of seismic and aseismic processes in the aftershock sequence. Moreover, we estimate aftershock migration rates and perform clustering analysis of the enhanced catalog to highlight finer-scale fault structures that were likely affected by Coulomb failure. Finally, to validate our analysis and monitor longer-term changes in physical mechanism contribution, we model the background seismicity across different zones of the Noto Peninsula using events from the 2020–2025 JMA catalog.

2. Methods

2.1. Pore fluid pressure modeling

To model the pore fluid pressure and fault strength evolution at the depth of the mainshock's hypocenter since the onset of diffuse seismicity in late 2020 (Peng et al., 2025), we followed the approach of Malagnini et al. (2012). This method assumes that the fault strength was purely hydrostatic before the time of interest. Because the pore fluid pressure coefficient (ratio of pore pressure to lithostatic pressure) can vary widely in hydrothermal and subduction zone systems (0.5–1.0; Bhowmick et al., 2024; Seno, 2009), we tested values between 0.6 and 1.0. We assume a static friction coefficient of 0.4, rock and fluid densities of 2990 and 1000 kg/m^3, respectively, and that the system is in a non-steady-state to account for large changes in pore fluid pressure. We

assume wet conditions to calculate the evolution of fault strength on a 41° dipping thrust fault using the equations described in Text S1a. The dip angle was chosen from the nodal plane determined by the United States Geological Survey (USGS) focal mechanism that best fits the observed seismicity. We use the injection point location and diffusivity (D) values of 0.1 and 0.2 m^2/s from Peng et al. (2025). The 3D distance from the injection point is used in our calculations. To evaluate the change in fault strength at the time of the M_w 7.5 mainshock, we take the fault strength at the time of the M_w 6.3 in 2023 as the initial value and subtract the subsequent values from it. More details about the methodology we used for our pore fluid pressure modeling can be found in Text S1a.

2.2. Coulomb stress changes

To evaluate the static stress changes caused by foreshocks, the 2024 mainshock, and aftershocks, we used the Coulomb 3.4.2 software (Toda et al., 2011). In this software, the change in Coulomb failure stress at a particular location or receiver fault is evaluated using the following equation:

$$\Delta CFS = \Delta\tau + \mu' \Delta\sigma \quad (1)$$

where $\Delta\tau$ and $\Delta\sigma$ are the changes in shear and normal stress, respectively. We assumed an effective friction coefficient (μ') of 0.4 for all our calculations. We used the model from Xu et al. (2024) as the input fault for the mainshock calculation. We selected all $M \geq 5$ events from our relocated catalog (see the subsequent section) for the aftershocks calculation. We generated fault geometries using the USGS's moment tensor fault parameters with lengths and widths based on the empirical relations from Wells and Coppersmith (1994), assuming the fault type is not known. We then evaluated their cumulative ΔCFS at the average depth of the aftershocks (10.60 km). For the foreshocks that occurred since the 2023 M_w 6.3 Noto earthquake, we used all $M \geq 5$ events from the JMA catalog. We evaluated their cumulative ΔCFS at the depth of the mainshock hypocenter (15.86 km). The fault slip model we used for the 2023 M_w 6.3 event was from Liu et al. (2024). For the other events, we used the strike, dip, and rake of the USGS moment tensor for the 2023 M_w 6.3 event (59, 44, and 99°, respectively) and the empirical relations from Wells and Coppersmith (1994) to obtain the length and width for faults of unknown type. The receiver fault we assumed for the foreshock calculation uses the USGS moment tensor parameters for strike, dip, and rake (49, 41, and 102°, respectively). For the main and aftershock calculations, we used optimally oriented thrust faults as the receiver. Coulomb 3.4.2 defines optimally oriented faults as those with strikes and dips that maximize the ΔCFS caused by an assumed source fault with an assumed regional stress tensor and μ' value for the receiver fault. We use the stress tensor from the stress map of Uchide et al. (2022) that is closest to the epicenter of the 2024 mainshock. To verify the robustness of our results, we varied the assumed calculation depths and effective friction coefficient (Text S1b).

2.3. Earthquake detection

To identify earthquakes potentially missing from the JMA catalog, we applied the template-matching approach of Vuan et al. (2018). This method utilizes waveform recordings of known earthquakes (template events) to scan streams of continuous data. For each template event, cross-correlation (CC) functions from multiple stations are synchronized based on S-wave arrival times and summed to obtain a stacked network function. In the CPU version of the code, a new detection is registered when the function exceeds a user-defined threshold, set as N times the daily median absolute deviation (MAD). To speed up the computation, we used the GPU version, which uses the mean CC across multiple channels to register a new detection.

Our templates consisted of JMA events within 100 km of the 2024 mainshock's epicenter, occurring between 2024/01/01 16:10:22 and 2024/02/02 00:00:00 and at depths shallower than our assumed crust-mantle boundary (29.5 km) of the velocity model (Ueno et al., 2002; Figure S1). This resulted in 19,694 template events.

To generate the template recordings, continuous waveform data from 62 Hi-Net three-component seismometers (Fig. 1) were downsampled from 100 Hz to 20 Hz for efficiency. After only keeping templates whose waveforms had sufficient signal-to-noise ratio on at least 4 seismogram components (see Text S1c), this left 19,686 templates to be used for detection. We employed a GPU-based template-matching implementation (Sugan et al., 2023) for detections in the 2–8 Hz band. The frequency range is selected based on mean inter-station and station-event distances to optimize detection capability. Detections required a mean CC $\geq$ 0.3 across at least four channels and a minimum separation of six seconds between consecutive detections. We then removed events that had $N < 8$ and mean CC $\geq$ 0.3 across fewer than 5 channels. More methodology details and justifications for the detection parameters can be found in Text S1c.

2.4. Earthquake relocation

We relocated the detected events using GrowClust (Trugman and Shearer, 2017), a hierarchical clustering algorithm that iteratively refines event locations based on differential travel times between pairs of events with similar P and S waveforms. Each event is paired with the 200 nearest detections within 5 km of the event using the ph2dt software of HypoDD (Waldhauser, 2001), with CC coefficients calculated using Fast Double-Difference Cross-Correlation (FDTCC) (Liu et al., 2022a, 2022b). FDTCC defines CC as the cross-correlation between P and S phase windows of two stations based on a user-defined threshold of time before and after the phase arrivals. We use a 1-second window before and after the phase arrivals. Only event pairs with at least six P/S-phase windows with CC $\geq$ 0.65 were selected for relocation with GrowClust. How uncertainty is determined as well as justifications for the selected relocation parameters can be found in Text S1d.

2.5. Comparing earthquake catalogs

To visualize the magnitude range at which new events are being added, we plotted the magnitude-frequency distributions of both the JMA and our relocated catalog (Figure S2). Additionally, we calculated the match rate of our catalog with the JMA catalog by first converting event coordinates in each catalog from spherical (Longitude, Latitude, Depth) to cartesian (Universal Transverse Mercator). Then, we iterated over all events in the JMA catalog, searching for events in our catalog that were within 3 s and 3 km of a particular event in the JMA catalog. This helps highlight how many of the events in our catalog are newly detected.

2.6. Clustering and orientation for coulomb failure

To examine clusters of earthquakes that are spatially close, we employed the Density-Based Spatial Clustering of Applications with Noise (DBSCAN) algorithm (Ester et al., 1996). DBSCAN will group points of sufficiently high density together and label the rest of the points as noise. We required that a given cluster have at least 75 events, and the maximum distance between two samples for them to be considered part of the same neighborhood (the parameter ε) was 1.0 km. We conduct sensitivity tests of the DBSCAN parameters in Text S1e. The fault planes were then fitted to the resulting clusters using the algorithm from Ross (2024). This algorithm iterates over a range of specific fault orientations, treating each fault as a cylindrical volume with a characteristic half-height (t) and radius (r_c). We have chosen $t = 0.4$ and r_c=4 km, following the r_c/t ratio from Ross (2024). For each point in the cluster, the algorithm centers a cylinder and counts the number of other points that fall within it. The orientation with the highest cumulative

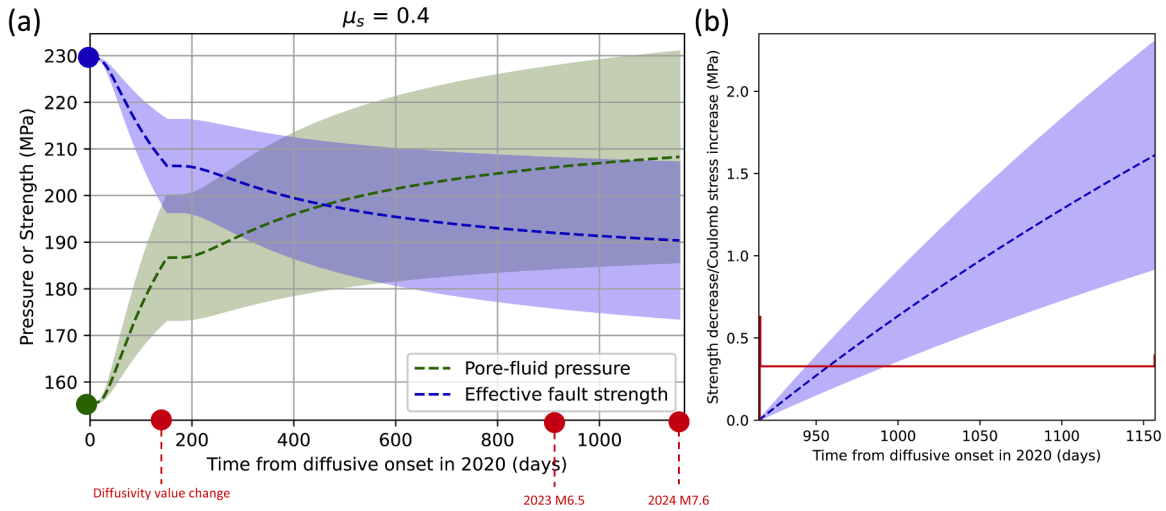

Fig. 2. (a) Pore fluid pressure (increasing green line) and fault strength (decreasing blue line) over time at the location of the 2024 M_w 7.5 mainshock with associated uncertainties due to using pore fluid pressure coefficients ranging between 0.6–1.0. Green and blue dots on the vertical axis correspond to the hydrostatic pressure and strength, respectively. The green and blue-dashed lines are calculated assuming a pore fluid pressure coefficient of 0.8. The red dots on the horizontal axis correspond to the timing of the change in diffusivity value from Peng et al. (2025), and the origin times of the 2023 M_w 6.3 and 2024 M_w 7.5 earthquakes. (b) Fault strength decrease (increasing blue dotted line) and the cumulative Coulomb stress change (red line) between the 2023 M_w 6.3 and 2024 M_w 7.5 earthquakes. The cumulative Coulomb stress change is calculated at the location of the 2024 M_w 7.5 mainshock for each M5+ earthquake that occurred between the two large earthquakes, assuming a receiver fault geometry of strike = 49°, dip=41° and rake=102° from USGS's focal mechanism. A zoom-in of the ~10 days since the 2023 M_w 6.3 event can be found in Figure S7. A map view of the cumulative Coulomb stress changes shown in (b) is plotted in Figure S19b.

count is considered the best-fitting fault plane.

Uchide et al. (2022) inverted focal mechanisms from 220,000 microearthquakes to obtain a nationwide stress map for Japan, providing stress tensors at every 0.2° interval. Using this data, we found the deviation (θ) of the normal vector of our fitted fault planes from the maximum principal stress direction of the closest stress tensor to a cluster's centroid. The following equation, based on Mohr-Coulomb theory, from Sibson (1974) and Twiss and Moores (2007):

$$\mu = \frac{1}{tan(2\theta)} \tag{2}$$

allowed us to then estimate a value for the coefficient of friction (μ) for each fault plane, assuming no cohesion. If the obtained μ value is between 0 and 1, then we define the cluster as in the reasonable range for Coulomb failure.

2.7. Spatiotemporal evolution of seismicity

Seismic migration speeds were estimated by projecting all events onto the USGS-assumed strike and dip (49° and 41°, respectively) of the mainshock fault plane. We assumed the seismicity occurred on a fault plane extending 70 and 97 km NE and SW (black-dotted line in Fig. 1). We exclude earthquakes that are in the ~7 % most distant from this assumed fault plane. This threshold was determined by calculating the 3-D distance from each event onto the USGS-determined strike and dip of the mainshock fault plane. The 90th percentile of the resulting distribution of distances (Figure S3c) is ~30 km, located just outside the bulk of the distribution. So, excluding all events with a distance greater than this removes outliers from the projection, amounting to 7 % of the resulting catalog. Each event's along-strike and along-dip distance relative to the mainshock was computed.

2.8. Seismic to geodetic moment ratio calculation

Discrepancies between seismic and geodetic moments can indicate aseismic slip. We estimated the seismic moment (M_0) of an earthquake using:

$$M_0 = 10^{1.5(M_L+9.05)} \tag{3}$$

where M_L is the local magnitude of an earthquake estimated by template matching.

The geodetic moment of each slip patch in the co- and 19-day postseismic slip models from Yang et al. (2024; Figure S4) was obtained by multiplying the area of a patch by its slip value and an assumed rigidity value (30 GPa). We compared seismic and geodetic moments for each patch in the northeast and southwest fault segments. For the seismic moment, we summed the seismic moments of earthquakes above/below the fault patches and within 20 km of the patch at 3 and 19 days post-mainshock (days 0–4 and 4–19, respectively).

2.9. Deep gaussian process epidemic type aftershock sequence (DGP-ETAS) modeling

To investigate the temporal evolution of the background seismicity μ_b, we employed the Deep Gaussian Process Epidemic Type Aftershock Sequence (DGP-ETAS) approach from Muir and Ross (2023). The typical Epidemic Type Aftershock Sequence (ETAS) parametric-based modeling approach (Ogata, 1988, 1998) assumes that seismic events are primarily caused by aftershock triggering with a fixed background seismicity rate that can be solved using the Maximum Likelihood Estimation (MLE). This means that it is challenging to model the seismicity rates of more complex sequences, such as fluid-driven swarms, which have a variable μ_b (Hainzl and Ogata, 2005; Kumazawa and Ogata, 2013; Llenos et al., 2009). Kumazawa and Ogata (2013), Marsan et al. (2013) and Trugman et al. (2016) expanded on this system to allow for temporal evolution in background rates, thus enabling the study of sequences with significant fluctuations in background seismicity rates (e.g., swarms). More recently, Muir and Ross (2023) implemented a DGP-based approach for determining the temporal evolution of background seismicity rates. The DGP-ETAS approach assumes time-varying μ_b, which may or may not be swarm-driven. The DGP builds on the semi-parametric single GP implementation by Molkenthin et al. (2022) by allowing for more abrupt changes in the rate to be detected. Some extra details about the DGP-ETAS method can be found in Text S1f.

We used earthquakes in the JMA catalog $M \geq 2.5$ occurring between

2020/01/01 and 2025/03/07 in our study region. This magnitude threshold was chosen based on computational limitations. Although excluding lower-magnitude events may reduce observable triggering information, DGP-ETAS propagates the resulting uncertainty through posterior credible intervals that may widen under sparse observational conditions.

For this complex sequence, the seismic swarm has largely been restricted to the northeast portion of the peninsula from 2020–2024. It was only after the nucleation of the 2024 mainshock that seismicity appeared northeast and southwest of the central zone. To investigate how differing mechanisms may have driven seismicity over space, we split the catalog into 3 different sub-regions as indicated in Figure S5 (southwest; SW, central; C, northeast; NE). These were chosen so that the central region of swarm activity was separated from the surrounding areas that saw little to no seismicity during the 2020–2024 swarm. Each sub-region was separated by a buffer zone to minimize the influence of physical mechanisms from neighboring sub-regions and contained 1706, 1455, and 1021 events, respectively. To obtain reference parameters for the model priors, we followed the approach from Muir and Ross (2023), which used Statistical Analysis of Point Processes with R (SAPP; Ogata, 2006) to model the typical ETAS (constant μ_b) seismicity rate in our study region (36.746–38.246°N, 136.52–138.02°E) between 2010 and 2020. The reference parameters and the associated model we obtained are shown in Figure S6. We assumed all the same sampling parameters as in Muir and Ross (2023) for each Gaussian layer.

3. Results

3.1. Contribution of coulomb stress and pore fluid pressure to the nucleation of the 2024 mainshock

The results of the pore fluid pressure calculations in Fig. 2a show that the effective fault strength decreased by about 40 ± 15 MPa from the beginning of fluid injection in 2020 to 2024. Zooming into the time range between the 2023 and 2024 mainshocks (Fig. 2b), we find that the effective fault strength decreased by about 1.6 ± 0.7 MPa. This is three times the Coulomb stress increase of ~0.4 MPa caused by all events $M \geq 5$ since the 2023 event, suggesting that pore fluid pressure changes since 2023 still played a significant role in bringing the 2024 mainshock's fault closer to failure. To validate our result, we varied the assumed coefficient of friction (Text S1a, Figures S7-S10) and found that the effective fault strength decrease consistently exceeds the Coulomb stress increase caused by all events $M \geq 5$ since the 2023 event.

3.2. Spatiotemporal evolution of seismicity one month before and after the 2024 earthquake

Using 19,686 template events from the JMA catalog, we detected 138,889 events and assigned them the same locations as their associated templates. The match rate of this catalog with JMA was ~97 %. These events were then relocated using the GrowClust software. Our final catalog contained 44,498 events, compared to the original 20,356 in the JMA catalog during the same time period. Most of our final catalog's new events are in the lower magnitude ranges of 0–2 (Figure S2). The match rate of our relocated catalog with JMA's was ~79 %, suggesting that our catalog contains 28,506 previously undetected events. Some JMA events were missed in our final catalog due to not meeting the criteria for relocation (see Methods). The match rate in the month before the mainshock was lower than that of the month after the mainshock (~39 % compared to ~80 %). This is expected as we only used aftershocks as templates. Figure S3a-b shows that our relocated catalog's location errors are relatively low (average of ~400 m). Additionally, the seismicity generally gets deeper as you go from southwest to northeast (Fig. 1) even if the depths are perturbed by their error bars (Figure S11), towards the Amur-Okhotsk plate boundary. This boundary has been interpreted as a developing or nascent convergence zone (Nakamura, 1983), so the depth of seismicity increasing as it approaches the boundary could be indicative of a developing subduction zone.

Examining the results of our projection onto the USGS-based fault plane, we find that the foreshocks in the month before the mainshock are mainly concentrated close to the mainshock's hypocenter in the northeast part of the Noto peninsula, where the ~4 year-long swarm had been occurring. We also see that the aftershock seismicity migrates northeast in the central zone, southwest in the southwest zone, and up/down-dip in both the central and SW zones along fronts of ~4.4 and 3.3 km/decade. Aftershock migration has been reported to follow a log(t) relationship with slopes in the range of 0.7–31 km/decade in the case of aseismic afterslip (Kato and Obara, 2014; Perfettini et al., 2019; Sugan et al., 2019). Near the Noto Peninsula, it has been reported in the range of 1–7 km/decade (Kato and Obara, 2014; Takahashi et al., 2026).

3.3. Seismic to geodetic moment ratios

Yang et al. (2024) obtained co and 19-day postseismic slip models of the earthquake using Global Navigation Satellite System (GNSS) data (Figure S4). We overlaid our seismicity on these slip models (Fig. 4a-b) and found that the peak seismicity density on both the northeastern and southwestern fault segments for the coseismic slip model is located near the main slip patch's edges. This is expected because the mainshock's principal fault patches relieve stress after the earthquake and trigger stress in the surrounding patches. This is shown in Figure S12, where the coseismic slip model's positive Coulomb stress change map on optimally oriented thrust faults coincides with zones of peak seismicity in the southwest, central and northeast zones. For the postseismic model, we also find that the peak seismicity density is located on the main slip patch's edges, which is to be expected as afterslip-induced deformation would load the surrounding parts of the fault. In this case, the stress map shown in Figure S12 indicates that the zones of peak seismicity density in both the northeast and central regions align well with areas of positive Coulomb stress change. In the southwest region, several zones of peak seismicity density zones coincide with positive stress changes. This overall pattern persists even after we varying the parameters used in the Coulomb stress calculations, as demonstrated in the robustness tests for the stress change maps (Text S1b; Figures S13-S15).

The seismic-to-geodetic moment ratio results in Fig. 4c highlight that the SW segment had generally higher ratio values than the NE segment (~4 % compared to 0.6 %). Both the NE and SW segments had a shallow portion of low ratio values, with higher values at intermediate depths. This, combined with the ΔCFS of the slip models (Figures S12-S15), suggests a combination of seismic and aseismic processes occurring in this aftershock sequence. Namely, the peak density of 4–19-day aftershocks is located above zones of $\Delta CFS > 0$ in the NE. In the SW, they are located near the slip patch's edges but not fully above zones of $\Delta CFS > 0$.

3.4. Clustering and coulomb stress

Using the DBSCAN algorithm allowed us to identify 21 clusters of earthquakes (larger dots in Fig. 5). After eliminating clusters whose fault geometry is highly uncertain, we find that 7 of the 21 clusters are in the orientation range for Coulomb failure, with 6 of the 7's μ values being around 0.1–0.2 and 1 having a value of ~0.8 (Fig. 5). When we overlay the positive ΔCFS zones from the finite model of the mainshock (Xu et al., 2024), we find that most of the 7 clusters are in the zones of positive ΔCFS values caused by the mainshock (Figure 5; Figures S16-S18 for robustness validation) or large aftershocks (Figure S19a). Almost all the clusters that are in the reasonable orientation range for Coulomb failure ($0 < \mu < 1$) are in the SW zone. Around half of the clusters not in the reasonable range for Coulomb failure are located outside regions of positive ΔCFS. Sensitivity tests of the DBSCAN and Coulomb stress parameters (Text S1b, S1e; Figures S20–31) led to similar results for the friction values. Additionally, most of the clusters in the reasonable range for Coulomb failure are still found in positive

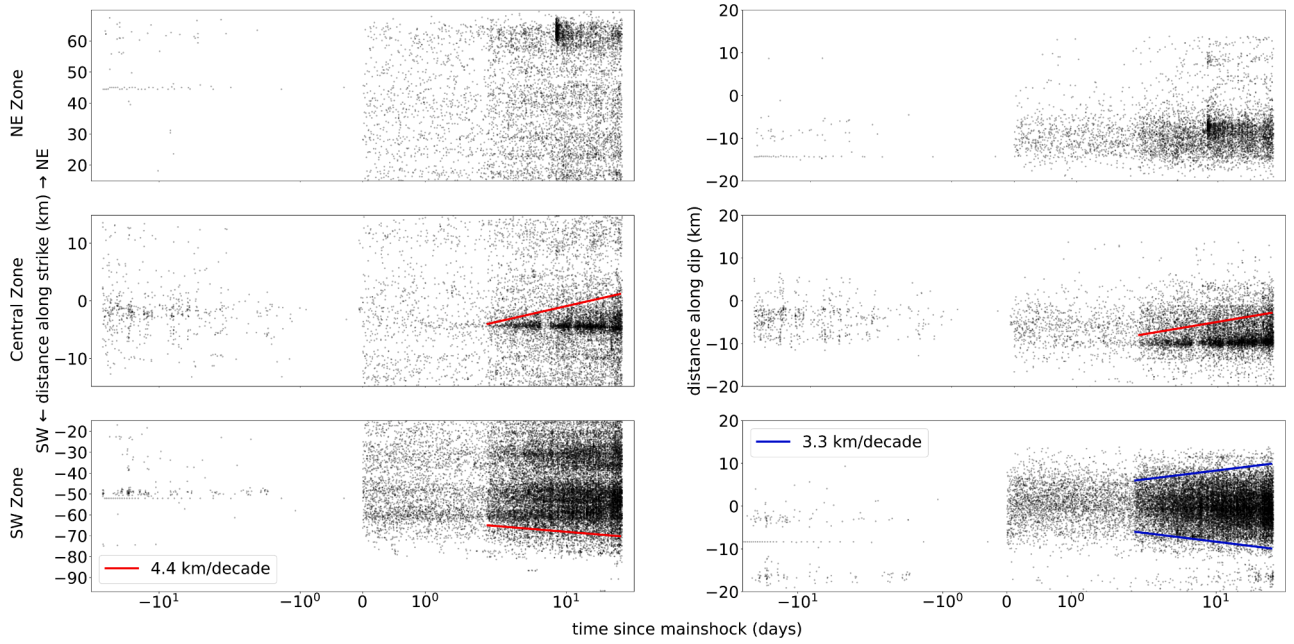

Fig. 3. Spatiotemporal evolution of our seismicity results along strike (left panel) and (right panel) along dip (angle = 41°) of the black dotted line in Fig. 1, with respect to the location of the mainshock. Plots are shown in log-linear scale. Positive dip direction corresponds to increasing depths. Red and blue lines show afterslip relations at expansion rates of 4.4 and 3.3 km/decade, respectively.

Δ*CFS* regions in the southwest and/or central zones, demonstrating the consistency of our results.

Those clusters that were not in the reasonable range for Coulomb failure and occur outside of areas of positive Δ*CFS* may have been driven by some other mechanism, such as afterslip. When we overlay the clustering from Fig. 5 onto the stress map associated with Yang et al. (2024)'s postseismic slip model at various depths (Figure S32), we find that around 4 of those clusters coincide with regions of positive ΔCFS caused by that slip model. This was consistent even after we varied the frictional parameter (Figures S33-S35). An approach that a future study may use to further verify the contribution of afterslip is to search for repeating earthquakes and examine whether accelerating slip rates were observed offshore following the 2024 mainshock. For unfavorably oriented clusters located in regions of positive Coulomb stress change, the inferred friction values may be overestimated due to the assumption of zero cohesion. This assumption implies that all faults are mature, whereas some of these clusters may represent immature faults that would be favorably oriented for failure if cohesion were considered. Immature fault zones tend to have a distributed network of damage, while mature fault zones are more localized (Thakur and Huang, 2021) as the fault evolves and reduces its geometrical complexity. Takahashi et al. (2026) show that seismicity in the southwest zone revealed complex small-scale fault structures but lacks the large aftershock plane associated with the 2007 M_w 6.7 Noto Hanto earthquake. It is therefore likely that those clusters are associated with immature faults that would require an estimate for the cohesion. Another mechanism for driving aftershocks in unfavorably oriented clusters is an increase in fault-confined fluid pressure, as found in Terakawa et al. (2013)'s study of aftershocks after the 2011 Tohoku-oki earthquake. Additional limitations include uncertainties in the regional stress tensor (from Uchide et al., 2022) and receiver fault geometry used in the Δ*CFS* calculations. Nonetheless, this approach serves as a first-order validation of the Δ*CFS* model and suggests that most favorably oriented faults likely consist of weaker materials, requiring lower stress to fail.

3.5. Validation with the background rate of the JMA catalog

Our results in Fig. 6 indicate that the SW and NE zones have an almost constant background rate despite increased seismicity in 2024. This suggests that seismicity in those regions follows a typical mainshock-aftershock system. However, the results for the central zone show a significant fluctuation in the background rate. Namely, we see the increase in background rate in mid-2021 with slight variations during upticks in seismicity, corresponding to the pre-2024 swarm activities. This is consistent with the results from Kumazawa and Ogata (2024b), who used a nonstationary ETAS modeling approach (Kumazawa and Ogata, 2024a) to solve the time-varying background rate and aftershock productivity. Our results, which extend into 2025, reveal a decrease in the background rate to pre-swarm levels following the 2024 mainshock. This could indicate a swarm cessation mechanism in the central zone.

3.6. Discussion

From our pore fluid pressure analysis, a 40 ± 15 MPa decrease in fault strength is reasonable for the time span we are looking at. Malagnini et al. (2012)'s study calculated a 7–10 MPa decrease in fault strength over 1–4 days at a similar depth (10 km). In our case, this value is over 4 years of a swarm. Our ~230 MPa initial effective fault strength, while high, is plausible. Behr and Platt (2014) suggest that while shallow brittle faults are weak, the more ductile middle crust can sustain higher effective frictional strength. Other studies suggest that pore pressure may approach lithostatic values at depth or may vary due to fault valve behavior, thereby keeping effective fault strength relatively low and less depth dependent (Zencher et al., 2006; Zhu et al., 2020). The fault we are working with also may have already been previously weakened by historical seismicity, so the initial value might be overestimated. Furthermore, our analysis assumes a constant friction parameter, which may not hold over the time scale considered. Frictional properties can evolve due to fluid migration and stress redistribution, potentially influencing our estimate of fault strength. However, the point of this calculation is more to assess the change in fault strength due to fluids compared to the increase in Coulomb stress due to foreshocks as opposed to constraining absolute values. Consequently, our results provide evidence that the 2024 M_w 7.5 Noto earthquake was primarily driven by pore fluid pressure buildup, with Coulomb stress changes generated by

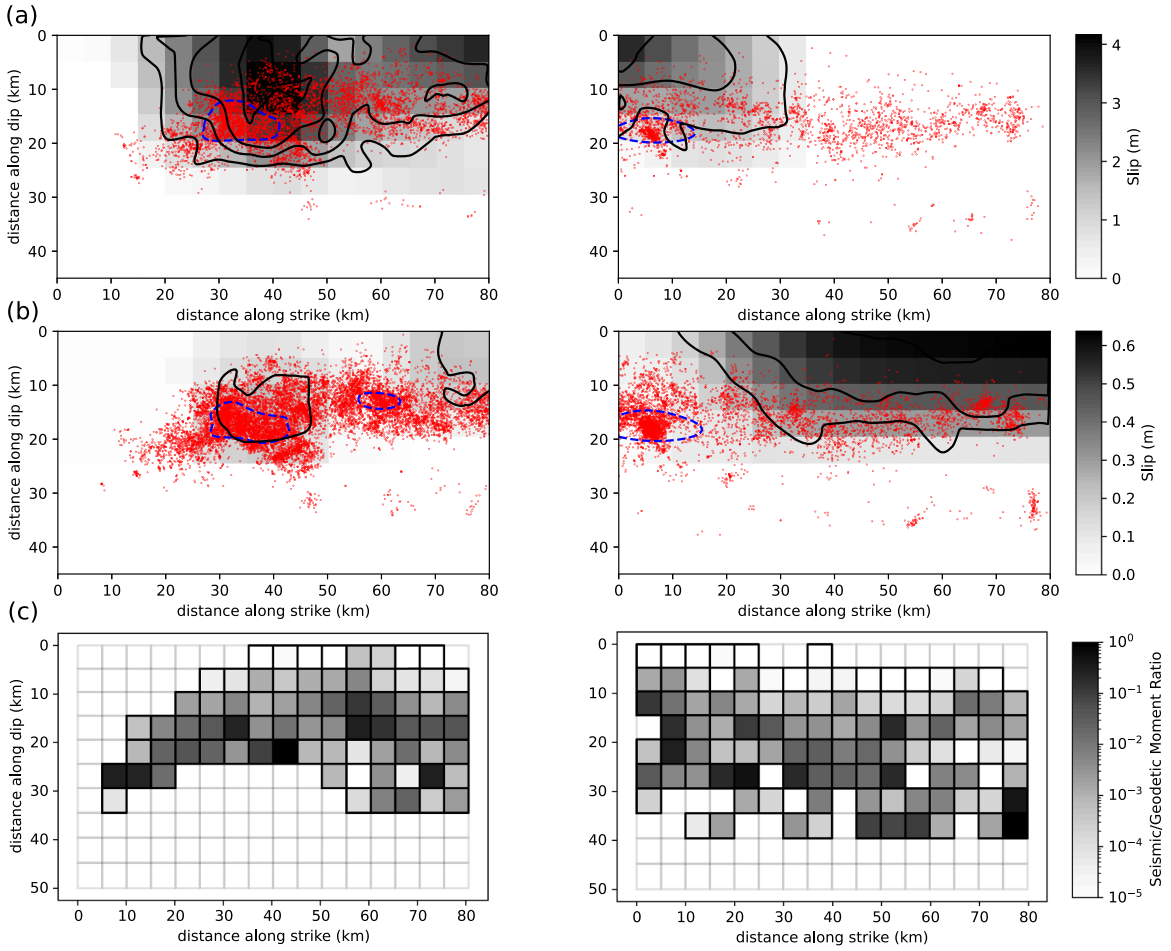

Fig. 4. (a) co- and (b) 19-day post-seismic slip models from Yang et al. (2024) with 3- and 19-day (days 0–4 and 4–19, respectively) aftershocks overlaid as red dots. The blue dashed circles show peak seismicity densities. Black lines show interpolated contours at (a) 1 and (b) 0.2 m intervals, respectively. A map view of the slip models can be found in Figure S4. (c) 19-day seismic-to-geodetic ratio model using our catalog and the geodetically-derived slips in (b). Subfaults with non-zero values are outlined with solid black lines.

the 2023 M_w 6.3 earthquake playing only a minor role (Fig. 2). This may be indicative of loading of the shallower brittle crust by the more ductile middle-to-deep crust. Incorporating temporal variations in the friction parameter in future analyses could further validate and refine this interpretation.

Our aftershock analysis indicates different behaviors in different regions of the fault system. In all sub-regions studied, the early aftershocks were located near the edges of the major coseismic slip patch (Fig. 4), indicating that interaction between earthquakes was likely the primary driver. This was especially prevalent in the SW zone, where several seismicity clusters were in the orientation range for Coulomb failure.

Additionally, the seismic-to-geodetic moment ratios indicate that the portions of all zones exhibit some sort of aseismic process (Fig. 4c). The ratio between the seismic moment release rate and the plate-motion-derived moment release rate, also known as seismic coupling, can be used to infer seismic hazard along a fault (Clarke et al., 1998; Palano et al., 2018). Locked regions (high coupling) are accumulating stress that will eventually be released in the form of seismic slip during earthquakes. Unlocked regions (low coupling) account for plate motion through aseismic slip driven by fault creep. Typically, geodetic and seismic data are analyzed over long terms (e.g., years or decades) and are used to derive ratios between seismic and geodetic moment rates (Mazzotti et al., 2011; Sparacino et al., 2022). In our study, the seismic-to-geodetic moment ratios we obtain offer a snapshot of the coupling state of the fault segments. It is important not to over-interpret fine-scale heterogeneities in our results, as there are uncertainties in our earthquake locations and the slip model we are using. However, we can generally say that the shallow portion of both the NE and SW segments (with low ratio values) have lower coupling than its intermediate depths in the time period examined. For the intermediate depths, the seismicity there results both from the Coulomb stress perturbation of the co and postseismic slip, indicating that zone was fully locked previously (there was little to no seismicity in the decades prior) and is now at least partially locked and unlocking as time goes on. In the SW and central zones, the seismicity is the result of perturbation from the significant coseismic slip but also from migrating aseismic afterslip. Given the large amount of Coulomb Stress imparted on the NE zone without as much seismicity being triggered, the material in the intermediate-depth NE zone may have higher frictional strength and thus is more resistant to unlocking compared to similar depths in the SW.

The migration velocities in the central and SW zones reveal a clear afterslip front (Fig. 3), with rates consistent with previous studies of seismicity on the Noto Peninsula. However, in the SW zone, the peak seismicity densities do not align well with areas of postseismic positive Coulomb stress change (Figure S12). One possibility is that the afterslip most strongly influencing aftershocks in this region occurred predominantly within the first four days, making its contribution difficult to isolate from the dominant coseismic elastic-triggering effects. Alternatively, dynamic triggering may also have contributed to the occurrence

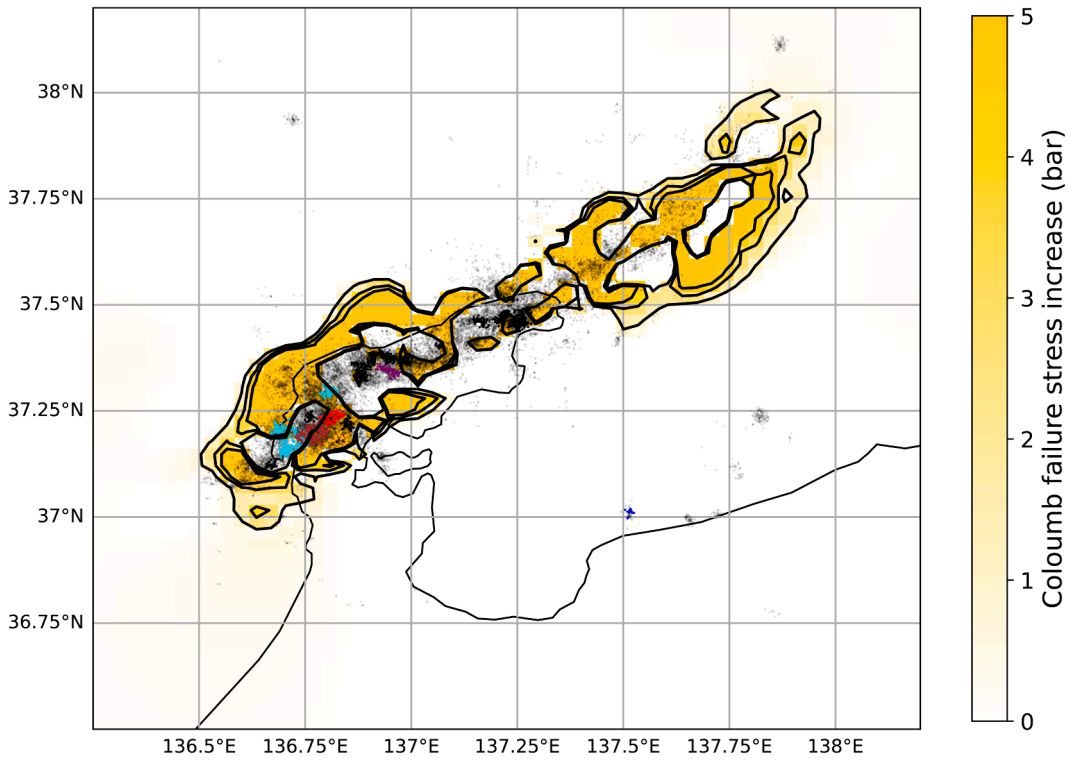

Fig. 5. Our obtained catalog (faint black dots) with clusters obtained from our DBSCAN analysis marked as larger dots. Black clusters were not found to be in the reasonable orientation range for Coulomb failure or had too much uncertainty in their fault orientations. Clusters with other colors had orientations within the reasonable range for Coulomb failure. We overlay regions of $\Delta CFS > 0$ in yellow, calculated from Xu et al. (2024)'s fault model at the average depth of the aftershocks using optimally oriented thrust faults as the receiver fault. All overlaid seismicity is at depths within 5 km of the calculation depth. Contours are shown at 0.1, 0.3, and 0.5 MPa intervals.

of these aftershocks. Despite the low ratio and significant postseismic slip observed in the shallow portion of the NE zone, there is no clear migration front evident in the NE, suggesting that the aseismic slip there is more localized. The decrease in the modeled background seismicity indicates that the central zone is showing signs of swarm cessation.

Several studies (Kato, 2024; Liu et al., 2024; Yoshida et al., 2023b) suggest that fluids upwelled from a zone near the crust-mantle boundary and progressively weakened the fault, eventually leading to the 2023 M_w 6.3 and 2024 M_w 7.5 earthquakes in the central zone. In particular, Kato (2024) proposes that this updip fluid migration follows the fault valve model (Sibson, 1992; Zhu et al., 2020), in which fluid pressures slowly increase in the interseismic period, eventually resulting in rock fractures that increase permeability and allow further diffusion and rock failure. Takano et al. (2024) support this interpretation and found that the seismicity occurring on the peninsula between 2018–2022 had largely occurred on optimally oriented faults relative to the regional stress field, save for a deeper cluster that likely tracked the updip migration of the fluid. The results of our DBSCAN-based analysis (Fig. 5) show that 2024 aftershock clusters in those locations occur on faults that are not optimally oriented for failure. Thus, these clusters may also be tracking the fluid diffusion. While this interpretation is plausible, the assumptions relating to Coulomb Stress and cohesion invite a stress-tensor-based post-2024 mainshock analysis, similar to that of Takano et al. (2024), so that this interpretation may be validated.

Given the cyclic nature of the fault valve model, it is possible that newly formed fracture pathways during the past four years of swarm

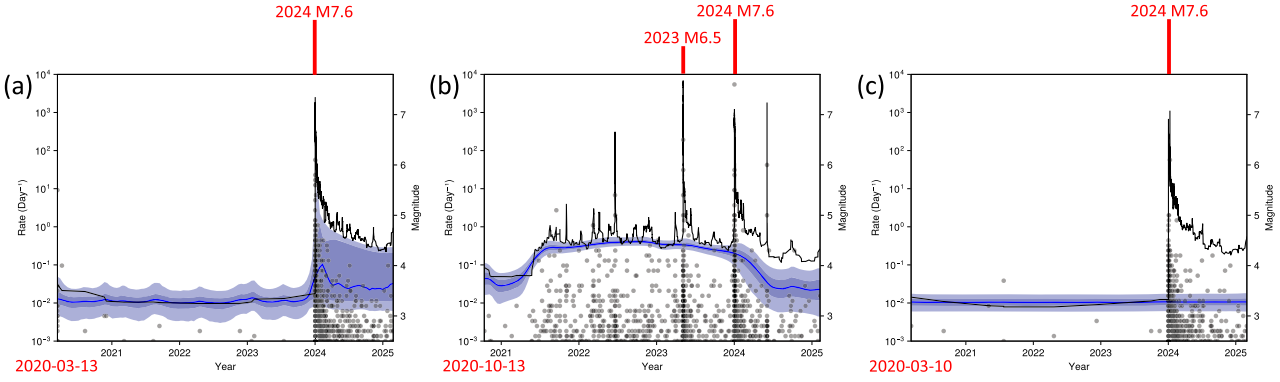

Fig. 6. DGP-ETAS results for background rate of the JMA earthquake catalog ($M \geq 2.5$) in the zone (a) southwest (SW), (b) center, and (c) northeast (NE) of the swarm region as indicated in Figure S5. For all plots, catalog events are shown as grey circles, and the 90 percent credible interval, 50 percent credible interval, and median of the posterior are shown in increasingly dark shades of blue. The first event date ($M \geq 2.5$) in the associated region is marked in red. The black line shows the total earthquake rate, smoothed over a 5-event window. The rates are plotted in log space.

activity enabled rapid diffusion of fluids into the surrounding rock, releasing the built-up pressure. In the long term, the fluid pressure can build up gradually while the swarm subsides. Given the modeled drop in background seismicity (Fig. 6), it is likely that the swarm cessation is dominant after the 2024 earthquake. This hypothesis is also supported by Yang et al. (2024), whose 19-day poroelastic rebound modeling predicted subsidence within the rupture area and uplift outside the rupture area, indicating possible migration of fluid away from the epicenter. On longer time scales (months to years), viscoelastic relaxation is expected to play a more dominant role in postseismic deformation (Chen et al., 2025). The initial poroelastic rebound may have facilitated fluid redistribution away from the rupture zone, contributing to long-term relaxation in the crust above the Noto Peninsula and potentially the significant postseismic slip seen in the shallow portion of the NE segment. Since our background seismicity results for the NE zone (Fig. 6c) do not show fluctuating background seismicity, as would be expected if there was a redistribution of fluids, we suggest that the poroelastic rebound effects are restricted to the central zone. This supports Yang et al. (2024)'s analysis that showed afterslip occurring in the weeks after the earthquake, with some near-field (closer to the central zone) subsidence explained by poroelastic rebound. Suito (2025) showed that not one mechanism (poroelastic rebound, afterslip, or viscoelastic relaxation) can fully explain the 100-day postseismic deformation at nearby geodetic stations. Note that the shallow NE portion did not experience coseismic slip or significant aftershocks. This could be indicative of a velocity-strengthening region that acts as a barrier to coseismic rupture and facilitates localized afterslip that triggers aftershocks in surrounding locked zones. This is evidenced by aftershocks being primarily located on the edges of the postseismic slip patch (Figs. 4b, 4c). Being near a partially convergent zone, this shallow zone of aseismic slip may indicate the location of a sediment-rich accretionary wedge. Further validation of this interpretation can be done by modeling the temporal evolution of the Omori-Utsu law parameters from ETAS in our different zones. Changes in aftershock productivity can indicate how the volume of brittle zones evolves (Dascher-Cousineau et al., 2020), helping to confirm the spatiotemporal distribution of seismic and aseismic processes in this four-year-long sequence.

4. Conclusion

Our high-resolution template matching catalog has allowed us to examine the spatiotemporal contributions of Coulomb failure, afterslip, and swarm activity during the 2024 M_w 7.5 Noto Peninsula earthquake sequence. We first showed that the elevated pore pressure was likely the primary trigger of the 2024 mainshock. Our subsequent seismicity analysis reveals that: 1) the southwest and central zones exhibit typical mainshock-aftershock behavior, where the seismicity is primarily driven either by the Coulomb stress changes or by aseismic afterslip, 2) the northeast zone's seismicity overlaps with areas of positive Coulomb stress change but has fewer signs of migrating aseismic afterslip, despite significant post-seismic deformation. Our findings from background seismicity evolution indicate a swarm-cessation mechanism in the central zone. We interpret this as the pressure-release phase of the cyclic fault valve model that leads to poroelastic rebound. Since the northeastern zone's background seismicity does not show signs of diffusive behavior related to the central zone's rebound, we attribute localized afterslip as the primary driver of the early northeastern postseismic slip.

Data availability

The continuous waveform data and JMA earthquake catalog are available for download with a free user account from https://www.hinet.bosai.go.jp/. Our obtained earthquake catalog is included in the supplement of this paper. The template matching codes we used are available in CPU (Sugan et al., 2023; Vuan et al., 2018) and GPU (Sugan et al., 2023) form. The ph2dt, FDTCC, and GrowClust relocation software are available from the LOC-FLOW algorithm (Zhang, 2022). The Python implementation of the pore fluid pressure modeling from Malagnini et al. (2012) can be provided upon request. Figures were generated with assistance from the Clawpack finite volume modeling software (Clawpack Development Team, 2024), Cartopy (Elson et al., 2024), and Matplotlib (Hunter et al., 2007).

Declaration of generative AI in scientific writing

During the preparation of this work, the author(s) used ChatGPT to improve the readability of parts of the article. After using this tool, the author(s) reviewed and edited the content as needed and take(s) full responsibility for the content of the published article.

Declaration of competing interest

The authors declare that they have no known competing financial interests or personal relationships that could have appeared to influence the work reported in this paper.

Acknowledgments

This work is supported by the NSF grants CAREER EAR-1848486 and EAR-2506181 (S.M., L.M.) as well as the NSFC Grant 42374056 (H.Y.). This work used computational and storage services associated with the Hoffman2 Cluster, which is operated by the UCLA Office of Advanced Research Computing's Research Technology Group. We thank the anonymous reviewers for their valuable comments that improved the quality of this article.

Supplementary materials

Supplementary material associated with this article can be found, in the online version, at doi:10.1016/j.epsl.2026.120113.

References

Amezawa, Y., Hiramatsu, Y., Miyakawa, A., Imanishi, K., Otsubo, M., 2023. Long-living earthquake swarm and intermittent seismicity in the northeastern tip of the Noto Peninsula. Jpn. Geophys. Res. Lett. 50, e2022GL102670. https://doi.org/10.1029/2022GL102670.

Behr, W.M., Platt, J.P., 2014. Brittle faults are weak, yet the ductile middle crust is strong: implications for lithospheric mechanics. Geophys. Res. Lett. 41 (22), 8067–8075. https://doi.org/10.1002/2014GL061349.

Bhowmick, S., Biswas, S.K., Mondal, T.K., 2024. Quantifying fluid pressure events using shallow crustal veins. Int. J. Earth Sci. (Geol Rundsch) 113, 145–160. https://doi.org/10.1007/s00531-023-02362-x.

Chen, Y., Li, J., Lu, K., Hu, T., 2024. Coseismic slip model and early post-seismic deformation processes of the 2024 M7.5 Noto Peninsula, Japan earthquake revealed by InSAR and GPS observations. Geophys. J. Int. 240 (2), 1048–1063. https://doi.org/10.1093/gji/ggae429.

Clarke, P.J., Davies, R.R., England, P.C., Parsons, B., Billiris, H., Paradissis, D., Veis, G., Cross, P.A., Denys, P.H., Ashkenazi, V., Bingley, R., Kahle, H.-G., Muller, M.-V., Briole, P., 1998. Crustal strain in central Greece from repeated GPS measurements in the interval 1989–1997. Geophys. J. Int. 135 (1), 195–214. https://doi.org/10.1046/j.1365-246X.1998.00633.x.

Clawpack Development Team (2024), Clawpack version 5.10.0, www.clawpack.org, doi:10.5281/zenodo.10896214.

Dascher-Cousineau, K., Brodsky, E.E., Lay, T., Goebel, T.H.W., 2020. What controls variations in aftershock productivity? J. Geophys. Res. 125 (2), e2019JB018111. https://doi.org/10.1029/2019JB018111.

Phil Elson, Elliott Sales de Andrade, Greg Lucas, Ryan May, Richard Hattersley, Ed Campbell, Ruth Comer, Andrew Dawson, Bill Little, Stephane Raynaud, scmc72, Alan D. Snow, lgolston, Byron Blay, Peter Killick, lbdreyer, Patrick Peglar, Nat Wilson, Andrew, Daniel Kirkham. (2024). SciTools/cartopy: REL: v0.24.1 (v0.24.1). Zenodo. doi:10.5281/zenodo.13905945.

Ester, M., Kriegel, H.P., Sander, J., Xu, X., 1996. A density-based algorithm for discovering clusters in large spatial databases with noise. In: Proceedings of the Second International Conference on Knowledge Discovery and Data Mining (KDD'96). AAAI Press, pp. 226–231. https://ui.adsabs.harvard.edu/link_gateway/1996kddm.conf.226E/PUB_PDF.

Gibbons, S., Ringdal, F., 2006. The detection of low magnitude seismic events using array-based waveform correlation. Geophys. J. Int. 165 (1), 149–166. https://doi.org/10.1111/j.1365-246X.2006.02865.x.
Gutenberg, B., Richter, C.F., 1944. Frequency of earthquakes in California. Bull. Seismol. Soc. Am. 34 (4), 185–188. https://doi.org/10.1785/BSSA0340040185.
Hainzl, S., Ogata, Y., 2005. Detecting fluid signals in seismicity data through statistical earthquake modeling. J. Geophys. Res. 110 (B5), 2004JB003247. https://doi.org/10.1029/2004JB003247.
Hunter, J.D., 2007. Matplotlib: a 2D graphics environment. Comput. Sci. Eng. 9 (3), 90–95. https://doi.org/10.1109/MCSE.2007.55.
Ishikawa, Y., Bai, L., 2024. The 2024 Mj 7.6 Noto Peninsula, Japan earthquake caused by the fluid flow in the crust. Earthq. Res. Adv. 4 (3), 100292. https://doi.org/10.1016/j.eqrea.2024.100292. ISSN 2772-4670.
Ishikawa Prefectural Government. (2024). Human and building damage caused by the 2020 Noto Peninsula Earthquake. Retrieved from https://www.pref.ishikawa.lg.jp/saigai/documents/higaihou_144_0709_1400.pdf [in Japanese].
Kato, A., Obara, K., 2014. Step-like migration of early aftershocks following the 2007 Mw 6.7 Noto-Hanto earthquake. Jpn. Geophys. Res. Lett. 41, 3864–3869. https://doi.org/10.1002/2014GL060427.
Kato, A., 2024. Implications of fault-valve behavior from immediate aftershocks following the 2023 Mj 6.5 earthquake beneath the Noto Peninsula, central Japan. Geophys. Res. Lett. 51, e2023GL106444. https://doi.org/10.1029/2023GL106444.
Kumazawa, T., Ogata, Y., 2013. Quantitative description of induced seismic activity before and after the 2011 Tohoku-Oki earthquake by nonstationary ETAS models. J. Geophys. Res. 118 (12), 6165–6182. https://doi.org/10.1002/2013JB010259.
Kumazawa, T., Ogata, Y., 2024a. Non-stationary ETAS model: how it works for external forcing. Seismol. Res. Lett. 95 (6), 3331–3342. https://doi.org/10.1785/0220240166.
Kumazawa, T., Ogata, Y., 2024b. Spatial and temporal variations of the 3-year earthquake swarm activities leading up to the M7.6 Noto Peninsula earthquake and interpretations of their activities. Earth. Planets. Space 76 (1), 164. https://doi.org/10.1186/s40623-024-02112-6.
Liu, M., Li, H., Li, L., Zhang, M., Wang, W., 2022a. Multistage nucleation of the 2021 Yangbi M S 6.4 earthquake, Yunnan, China and its foreshocks. J. Geophys. Res. 127, e2022JB024091. https://doi.org/10.1029/2022JB024091.
Liu, M., Li, H., Zhang, M., Wang, W., Yang, Y., Li, L., Chang, Z., Zhang, H., 2022b. Investigation of the 2013 Eryuan, Yunnan, China MS 5.5 earthquake sequence: aftershock migration, seismogenic structure and hazard implication. Tectonophysics 837, 229445. https://doi.org/10.1016/j.tecto.2022.229445. ISSN 0040-1951.
Liu, C., Bai, Y., Lay, T., He, P., Wen, Y., Wei, X., Xiong, N., Xiong, X., 2024. Shallow crustal rupture in a major MW 7.5 earthquake above a deep crustal seismic swarm along the Noto Peninsula in western Japan. Earth Planet. Sci. Lett. 648, 119107. https://doi.org/10.1016/j.epsl.2024.119107. ISSN 0012-821X.
Llenos, A.L., McGuire, J.J., Ogata, Y., 2009. Modeling seismic swarms triggered by aseismic transients. Earth Planet. Sci. Lett 281 (1–2), 59–69. https://doi.org/10.1016/j.epsl.2009.02.011.
Malagnini, L., Lucente, F.P., De Gori, P., Akinci, A., Munafo', I., 2012. Control of pore fluid pressure diffusion on fault failure mode: insights from the 2009 L'Aquila seismic sequence. J. Geophys. Res. 117, B05302. https://doi.org/10.1029/2011JB008911.
Marsan, D., Prono, E., Helmstetter, A., 2013. Monitoring aseismic forcing in fault zones using earthquake time series. Bull. Seismol. Soc. Am. 103 (1), 169–179. https://doi.org/10.1785/0120110304.
Mazzotti, S., Leonard, L.J., Cassidy, J.F., Rogers, G.C., Halchuk, S., 2011. Seismic hazard in western Canada from GPS strain rates versus earthquake catalog. J. Geophys. Res. 116, B12310. https://doi.org/10.1029/2011JB008213.
Molkenthin, C., Donner, C., Reich, S., Zöller, G., Hainzl, S., Holschneider, M., Opper, M., 2022. GP-ETAS: semiparametric bayesian inference for the spatio-temporal epidemic type aftershock sequence model. Stat. Comput. 32 (2), 29. https://doi.org/10.1007/s11222-022-10085-3.
Muir, J., Ross, Z., 2023. A deep Gaussian process model for seismicity background rates. Geophys. J. Int. 234 (1), 427–438. https://doi.org/10.1093/gji/ggad074.
Nakamura, K., 1983. Possible nascent trench along the eastern Japan Sea as convergent boundary between the Eurasian and North American plates. Bull. Earthq. Res. Inst. Univ. Tokyo 58, 711–722.
Nishimura, T., Hiramatsu, Y., Ohta, Y., 2023. Episodic transient deformation revealed by the analysis of multiple GNSS networks in the Noto Peninsula, central Japan. Sci. Rep. 13, 8381. https://doi.org/10.1038/s41598-023-35459-z.
Ogata, Y., 1988. Statistical models for earthquake occurrences and residual analysis for point processes. J. Am. Stat. Assoc. 83 (401), 9–27. https://doi.org/10.1080/01621459.1988.10478560.
Ogata, Y., 1998. Space-time point-process models for earthquake occurrences. Ann. Inst. Stat. Math. 50 (2), 379–402. https://doi.org/10.1023/A:1003403601725.
Ogata, Y., 2006. Statistical Analysis of Seismicity: Updated Version (SASeis2006), 33. Computer Science Monographs, The Institute of Statistical Mathematics, Tokyo of. https://www.ism.ac.jp/editsec/csm/pdf/csm_033.pdf.
Omori, F., 1894. On the aftershocks of earthquakes. J. Coll. Sci. Imp. Univ. Tokyo 7, 111–200.
Palano, M., Imprescia, P., Agnon, A., Gresta, S., 2018. An improved evaluation of the seismic/geodetic deformation-rate ratio for the Zagros Fold-and-Thrust collisional belt. Geophys. J. Int. 213 (1), 194–209. https://doi.org/10.1093/gji/ggx524.
Peng, Z., Lei, X., Wang, Q., Wang, D., Mach, P., Yao, D., Kato, A., Obara, K., Campillo, M., 2025. The evolution process between the earthquake swarm beneath the Noto Peninsula, central Japan and the 2024 M 7.6 Noto Hanto earthquake sequence. Earthq. Res. Adv. 5 (1), 100332. https://doi.org/10.1016/j.eqrea.2024.100332. ISSN 2772-4670.
Perfettini, H., Frank, W.B., Marsan, D., Bouchon, M., 2019. Updip and along-strike aftershock migration model driven by afterslip: application to the 2011 Tohoku-Oki aftershock sequence. J. Geophys. Res. 124, 2653–2669. https://doi.org/10.1029/2018JB016490.
Ross, Z., 2024. Insights on the dip of fault zones in Southern California from modeling of seismicity with anisotropic point processes. Seismica 3 (1). https://doi.org/10.26443/seismica.v3i1.1092.
Seno, T., 2009. Determination of the pore fluid pressure ratio at seismogenic megathrusts in subduction zones: implications for strength of asperities and Andean-type mountain building. J. Geophys. Res. 114, B05405. https://doi.org/10.1029/2008JB005889.
Shelly, D., Beroza, G., Ide, S., 2007. Non-volcanic tremor and low-frequency earthquake swarms. Nature 446, 305–307. https://doi.org/10.1038/nature05666.
Sibson, R., 1974. Frictional constraints on thrust, wrench, and normal faults. Nature 249, 542–544. https://doi.org/10.1038/249542a0.
Sibson, R.H., 1992. Implications of fault-valve behaviour for rupture nucleation and recurrence. Tectonophysics 211 (1–4), 283–293. https://doi.org/10.1016/0040-1951(92)90065-E.
Sparacino, F., Galuzzi, B.G., Palano, M., Segou, M., Chiarabba, C., 2022. Seismic coupling for the aegean-anatolian region. Earth-Sci. Rev. 228, 103993. https://doi.org/10.1016/j.earscirev.2022.103993.
Sugan, M., Vuan, A., Kato, A., Massa, M., Amati, G., 2019. Seismic evidence of an early afterslip during the 2012 sequence in Emilia (Italy). Geophys. Res. Lett. 46, 625–635. https://doi.org/10.1029/2018GL079617.
Sugan, M., Campanella, S., Chiaraluce, L., Michele, M., Vuan, A., 2023. The unlocking process leading to the 2016 Central Italy seismic sequence. Geophys. Res. Lett. 50, e2022GL101838. https://doi.org/10.1029/2022GL101838.
Suito, H., 2025. Postseismic deformation model of the 2024 Noto Peninsula earthquake, central Japan. Earth. Planets. Space 77, 100. https://doi.org/10.1186/s40623-025-02228-3.
Takahashi, H., Aoyagi, Y., Yoshida, K., Kimura, H., Kurashimo, E., Sakai, S., 2026. High-precision aftershock distribution highlights the complex fault geometry of the 2024 M_w 7.5 Noto Peninsula earthquake. Geophys. Res. Lett. 53 (4), e2025GL118413. https://doi.org/10.1029/2025GL118413.
Takano, S., Hiramatsu, Y., Yukutake, Y., 2024. The role of fluids in earthquake swarms in northeastern Noto Peninsula, central Japan: insights from source mechanisms. Earth. Planets. Space 76 (1), 151. https://doi.org/10.1186/s40623-024-02099-0.
Terakawa, T., Hashimoto, C., Matsu'ura, M., 2013. Changes in seismic activity following the 2011 Tohoku-oki earthquake: effects of pore fluid pressure. Earth Planet. Sci. Lett. 365, 17–24. https://doi.org/10.1016/j.epsl.2013.01.017.
Thakur, P., Huang, Y., 2021. Influence of fault zone maturity on fully dynamic earthquake cycles. Geophys. Res. Lett. 48 (17), e2021GL094679. https://doi.org/10.1029/2021GL094679.
Toda, S., Stein, R.S., Sevilgen, V., Lin, J., 2011. Coulomb 3.3 graphic-rich deformation and stress-change software for earthquake. tectonic, and Volcano Research and Teaching—User guide: U.S. Geological Survey Open-File Report 2011–1060, 63 p available at https://pubs.usgs.gov/of/2011/1060/.
Trugman, D., Shearer, P., 2017. GrowClust: a hierarchical clustering algorithm for relative earthquake relocation, with application to the Spanish Springs and Sheldon, Nevada, earthquake sequences. Seismol. Res. Lett. 88 (2A), 379–391. https://doi.org/10.1785/0220160188.
Trugman, D.T., Shearer, P.M., Borsa, A.A., Fialko, Y., 2016. A comparison of long-term changes in seismicity at the Geysers, Salton Sea, and Coso geothermal fields. J. Geophys. Res. 121 (1), 225–247. https://doi.org/10.1002/2015JB012510.
Twiss, R.J., Moores, E.M., 2007. Structural Geology (2nd ed, 736 p. W. H. Freeman and Company, New York.
U.S. Geological Survey. (n.d.). Google Earth™/KML files: earthquake hazards program. U.S. Dep. Inter.. Retrieved from https://www.usgs.gov/programs/earthquake-hazards/google-earthtmkml-files.
Uchide, T., Shiina, T., Imanishi, K., 2022. Stress map of Japan: detailed nationwide crustal Stress field inferred from focal mechanism solutions of numerous microearthquakes. J. Geophys. Res. 127 (6), e2022JB024036. https://doi.org/10.1029/2022JB024036.
Ueno, H., Hatakeyama, S., Aketagawa, T., Funasaki, J., Hamada, N., 2002. Improvement of hypocenter determination procedures in the Japan meteorological agency (in Japanese). Q. J. Seismol. 65, 123–134.
Utsu, T., 1961. A Statistical Study of the Occurrence of Aftershocks, 30. Geophysical Magazine, pp. 521–605.
Vuan, A., Sugan, M., Amati, G., Kato, A., 2018. Improving the detection of low-magnitude seismicity preceding the Mw 6.3 L'Aquila earthquake: development of a scalable code based on the cross correlation of template earthquakes. Bull. Seismol. Soc. Am. 108 (1), 471–480. https://doi.org/10.1785/0120170106.
Waldhauser, F., 2001. hypoDD-A Program to Compute Double-Difference Hypocenter Locations (Report 2001–113; Version 1.0, Open-File Report). USGS Publications Warehouse. https://doi.org/10.3133/ofr01113.
Wells, D., Coppersmith, K., 1994. New empirical relationships among magnitude, rupture length, rupture width, rupture area, and surface displacement. Bull. Seismol. Soc. Am. 84 (4), 974–1002. https://doi.org/10.1785/BSSA0840040974.
Xu, L., Ji, C., Meng, L., Ampuero, J.-P., Yunjun, Z., Mohanna, S., Aoki, Y., 2024. Dual-initiation ruptures in the 2024 Noto earthquake encircling a fault asperity at a swarm edge. Science 385 (6711), 871–876. https://doi.org/10.1126/science.adp0493.
Yang, S., Sang, C., Hu, Y., Wang, K., 2024. Coseismic and early postseismic deformation of the 2024 Mw 7.45 Noto Peninsula earthquake. Geophys. Res. Lett. 51, e2024GL108843. https://doi.org/10.1029/2024GL108843.
Yoshida, K., Uno, M., Matsuzawa, T., Yukutake, Y., Mukuhira, Y., Sato, H., Yoshida, T., 2023a. Upward earthquake swarm migration in the northeastern Noto Peninsula,

Japan, initiated from a deepring-shaped cluster: possibility of fluid leakage from a hidden magma system. J. Geophys. Res. 128, e2022JB026047. https://doi.org/10.1029/2022JB026047.

Yoshida, K., Uchida, N., Matsumoto, Y., Orimo, M., Okada, T., Hirahara, S., et al., 2023b. Updip fluid flow in the crust of the northeastern Noto Peninsula, Japan, triggered the 2023 Mw 6.2 Suzu earthquake during swarm activity. Geophys. Res. Lett. 50, e2023GL106023. https://doi.org/10.1029/2023GL106023.

Yuhi, M., Umeda, S., Arita, M., Ninomiya, J., Gokon, H., Arikawa, T., Mori, N., 2024. Post-event survey of the 2024 Noto Peninsula earthquake tsunami in Japan. Coast. Eng. J. 66, 405–418. https://doi.org/10.1080/21664250.2024.2368955.

Zencher, F., Bonafede, M., Stefansson, R., 2006. Near-lithostatic pore pressure at seismogenic depths: a thermoporoelastic model. Geophys. J. Int. 166 (3), 1318–1334. https://doi.org/10.1111/j.1365-246X.2006.03069.x.

Zhang, M., 2022. Dal-mzhang/LOC-FLOW: LOC-FLOW (v0.0.1). Zenodo. https://doi.org/10.5281/zenodo.5875084.

Zhu, W., Allison, K.L., Dunham, E.M., Yang, Y., 2020. Fault valving and pore pressure evolution in simulations of earthquake sequences and aseismic slip. Nat. Commun. 11 (1), 4833. https://doi.org/10.1038/s41467-020-18598-z.